

The ultra-diffuse galaxy NGC 1052-DF2 with MUSE: I. Kinematics of the stellar body[★]

Eric Emsellem^{1,2}, Remco F. J. van der Burg¹, Jérémie Fensch¹, Tereza Jerabkova^{1,3,4}, Anita Zanella¹, Adriano Agnello^{1,5}, Michael Hilker¹, Oliver Müller⁶, Marina Rejkuba¹, Pierre-Alain Duc⁶, Patrick Durrell⁷, Rebecca Habas⁸, Federico Lelli¹, Sungsoon Lim⁹, Francine R. Marleau⁸, Eric Peng^{10,11}, Rubén Sánchez-Janssen¹²

¹ European Southern Observatory, Karl-Schwarzschild-Str. 2, D-85748 Garching, Germany

² Univ Lyon, Univ Lyon1, ENS de Lyon, CNRS, Centre de Recherche Astrophysique de Lyon UMR5574, F-69230 Saint-Genis-Laval France

³ Helmholtz Institut für Strahlen und Kernphysik, Universität Bonn, Nussallee 1416, 53115 Bonn, Germany

⁴ Astronomical Institute, Charles University in Prague, V Holešovičkách 2, CZ-180 00 Praha 8, Czech Republic

⁵ DARK, Niels Bohr Institute, University of Copenhagen, Lyngbyvej 2, 2100 Copenhagen, Denmark

⁶ Observatoire Astronomique de Strasbourg (ObAS), Université de Strasbourg - CNRS, UMR 7550 Strasbourg, France

⁷ Youngstown State University, One University Plaza, Youngstown, OH 44555 USA

⁸ Institut für Astro- und Teilchenphysik, Universität Innsbruck, Technikerstraße 25/8, Innsbruck, A-6020, Austria

⁹ NRC Herzberg Astronomy and Astrophysics Research Centre, 5071 West Saanich Road, Victoria, BC, V9E 2E7, Canada

¹⁰ Department of Astronomy, Peking University, Beijing, China 100871

¹¹ Kavli Institute for Astronomy and Astrophysics, Peking University, Beijing, China 100871

¹² UK Astronomy Technology Centre, Royal Observatory, Blackford Hill, Edinburgh, EH9 3HJ, UK

Received December 18, 2018

ABSTRACT

NGC 1052-DF2, a so-called Ultra Diffuse Galaxy (UDG), has recently been the subject of intense debate; it was announced to be a galaxy lacking dark matter based on a spectroscopic study of its constituent globular clusters. Both the measurement of its distance as well as the (dependent) measurement of the dynamical mass have been disputed since. Here we present the first spectroscopic analysis of the stellar body of the UDG, using the exceptional capabilities of the MUSE@VLT integral-field spectrograph. The MUSE datacube simultaneously reveals an intriguing stellar velocity field for the UDG, and systemic velocities for seven globular clusters. We further discovered three Planetary Nebulae (PNe) which are likely part of this galaxy, a première for UDGs. While five of the clusters had velocities measured in the literature, we were able to confirm the membership of two more candidates through precise radial velocity measurements. The mean velocity of the diffuse stellar body, $1793 \pm 2 \text{ km s}^{-1}$, is consistent with the mean globular cluster velocity. We detect a weak but significant velocity gradient within the stellar body, with a kinematic axis close to the photometric major-axis, making it a prolate-like rotator. We estimate a velocity dispersion from the clusters and PNe of $\sigma_{\text{int}} = 10.5_{-2.2}^{+4.0} \text{ km s}^{-1}$. We also derive a velocity dispersion $\sigma_{\star}(R_e)$ for the stellar body within one effective radius of $16.3 \pm 5 \text{ km s}^{-1}$, though with a full range $[13 - 27] \text{ km s}^{-1}$ accounting for potential systematics. We provide updated mass estimates based on these dispersions corresponding to the different distances to NGC 1052-DF2 that have been reported in the recent literature.

Key words. Galaxy: kinematics and dynamics, Galaxy: stellar content, Galaxies: dwarf

1. Introduction

Low-luminosity galaxies are by far the dominant galaxy population in numbers and have been the target of extensive studies to probe the various formation channels that may be called upon (Mayer 2011; McConnachie 2012; Skillman 2012; Lelli et al. 2014). Recent works have revived the scientific debate making dwarf galaxies appear as potential Rosetta Stones for our understanding of the cosmological paradigm (see e.g. Oman et al. 2019). Going from the low- to high mass regimes of galaxies, it has been argued that the stellar mass build up mostly goes from in-situ to ex-situ (Oser et al. 2010; Clauwens et al. 2018). In other words, dwarfs tend to grow their stellar mass via internal star formation while galaxy mergers dominate the assembly of giant systems. Still, a common property for galaxies from low

to high masses is the derived high dynamical mass-to-light ratios, something that is generally interpreted as the presence of a significant fraction of dark matter. Another interesting emerging thread may be the existence at both extremes of a zoo of morphological and dynamical structures, with e.g., kinematically decoupled components, or more generally departures from oblateness (e.g. Krajnović et al. 2011; Battaglia et al. 2013; Toloba et al. 2014; Guérou et al. 2015), which illustrates a likely richness of evolutionary paths. Scrutinising the internal stellar kinematics of galaxies thus became an essential ingredient to constrain formation and evolution processes (see e.g., Cappellari 2017).

In such a context, two exceptional claims were made about NGC 1052-DF2, an Ultra Diffuse Galaxy (UDG) likely located between 13 Mpc and 20 Mpc from us (Trujillo et al. 2018; van Dokkum et al. 2018d). First, by using the relative velocity distribution of 10 spatially associated globular clusters (GC), van Dokkum et al. (2018c) inferred an internal velocity dispersion of less than 10 km/s for the UDG and argued for a lack of dark

* Based on observations collected at the European Southern Observatory under ESO programmes 2101.B-5008(A) and 2101.B-5053(A).

matter in this galaxy assuming a distance of 20 Mpc¹. Second, based on GC numbers and mass estimates, the GC system of NGC 1052-DF2 would be over-populated and contain more massive clusters compared to what is expected for galaxies of similar halo mass (van Dokkum et al. 2018a). These claims triggered heated debates in the community, related to the statistical methods (Martin et al. 2018), the distance estimation (Trujillo et al. 2018), the reliability of estimated masses (Laporte et al. 2018) and implications for modified gravity (Famaey et al. 2018; Kroupa et al. 2018). With current uncertainties, the mass estimates range from a starlight-dominated to a dark-matter dominated galaxy (Hayashi & Inoue 2018).

All of the above were based on multi-slit spectroscopy of 10 GCs, as no spectroscopic data were yet available for the stellar body of the UDG. The stellar populations, GC kinematic association, and internal velocity dispersion of the UDG were still unknown.

In this paper, we present the first spectroscopic observations of the stellar body of the UDG, obtained with MUSE at the VLT. This integral field spectrograph allowed us to simultaneously obtain the spectrum of seven associated GCs, two of which did not yet have a measured systemic velocity, as well as three newly discovered Planetary Nebulae (PNe). We used this unique dataset to consistently compare the receding velocities and stellar populations of the galaxy and its GC and PNe systems. We briefly present our data and analysis in Section 2, also describing our approach to extract the kinematics of the UDG, GCs and PNe. Results on the kinematics are presented in Sect. 3, and then discussed in Sect. 4. We briefly summarise and conclude in Sect. 5. A companion paper focuses on constraining the detailed properties of the associated stellar populations (Paper II, Fensch et al., subm.).

Throughout this paper, magnitudes are given in the AB system. Unless stated otherwise, error bars denote 1σ uncertainties, or 68% confidence/credibility intervals.

2. Data & Analysis

VLT/MUSE observations of NGC1052-DF2 were conducted via ESO-DDT programmes (2101.B-5008(A) and 2101.B-5053(A), PI: Emsellem) in service mode during dark-time periods from July to November 2018. Seven observing blocks (OBs) were executed, amounting to a total of ~ 5.1 h on-target integration time. Five OBs were observed with seeing between $\sim 0''.4 - 0''.6$ while the last two had seeing between $\sim 0''.7$ and $1''.0$, allowing us to study the galaxy out to 1.5 effective radii and down to a surface brightness of nearly 26 mag arcsec $^{-2}$ (I_{814} band), plus faint spatially unresolved GCs and PNe of NGC 1052-DF2 (DF2, hereafter). Each OB was split in four individual on target exposures with slight dithers and rotations to average out cosmic rays and patterns associated with the slicers. We deliberately off-set the MUSE field with respect to the centre of the galaxy by $\sim 8''$ to probe a region where the surface brightness of the UDG is several magnitudes fainter than at the centre (Fig. 1), and extract relevant spectral information for the sky background, as explained below. The first three OBs (July) had a "S O O S O O S" sequence (with S being offset skies, 180s each and O being the Object/Galaxy exposed for 637s each) while the last four OBS (November) had a "S O O O O S" sequence, with the same 180s on-sky exposures and slightly longer 672s exposures on target.

¹ Note that van Dokkum et al. (2018c) derived a value of 19 ± 1.7 Mpc, and adopted a distance of 20 Mpc for their study, subsequently refined as 18.7 ± 1.7 Mpc in van Dokkum et al. (2018d).

Offset skies were meant to serve as a rescue plan for the sky subtraction, but were ultimately used for consistency checks only.

2.1. Reduction steps

All MUSE OBs were reduced using the latest MUSE esorex pipeline recipes (2.4.2), all wrapped within a dedicated python package (pymusepipe, available via [github](https://github.com)). The reduction follows the standard steps (bias, flat, wavelength calibration, Line Spread Function, illumination), and produce the so-called Pixel Tables which are corrected for barycentric motion, combined and resampled after alignment using the `exp_combine` MUSE pipeline recipe.

The MUSE pipeline includes a wavelength calibration based on arc lamp exposures that were taken during the day, after correcting for the difference in temperature. The reported accuracy is around 0.03 Å (rms). The pipeline also corrects each exposure for any residual global shifts using the detected sky lines. We performed a consistency check using the positions of the sky lines in the object frames themselves, confirming that the resulting wavelength calibration is accurate within 2 km/s, and is uniform over the field-of-view of MUSE.

We identified and subtracted the sky background using the Zurich Atmosphere Purge ZAP software package (Soto et al. 2016), a Principal Component Analysis-based sky subtraction tool (developed by the MUSE GTO team) that is optimized for IFU instruments. The principal components (eigen-spectra) are derived from the outermost regions of the MUSE object cube, where the sky is dominant (see the blue region in the middle panel of Fig. 1), after masking fore- and background sources. We also experimented by letting ZAP set-up the eigen-spectra on the external sky exposures (and then fitting them to the object cube), but found an inferior performance compared to exclusively using the sky-dominated region in the object stack due to time variations in the sky background and the significantly shorter exposure time. Even though this is an area to investigate further, we speculate that the flat-fielding of MUSE is sufficiently good that sky regions that are observed at the exact same time, yet falling on a different place on the detector, are preferred over the offset exposures. In Appendix A we describe the tests we performed to ensure that the source spectra are not affected by ZAP.

2.2. Detection and spectral extraction

We extracted spectra for the globular clusters studied in van Dokkum et al. (2018c) (green circles in Fig. 1), as well as the globular cluster candidates reported in Trujillo et al. (2018) (blue and red circles in Fig. 1), that fall within the MUSE field of view. Furthermore, in order to detect possible planetary nebulae around DF2 we cut the cube in three slabs of 8 Å centered on the redshifted wavelength of the [O III] doublet and H α emission lines, from which we subtracted three slabs of the same width in spectrally close featureless regions. Three sources with unambiguous detection of the [O III] doublet and H α line were found. All GCs and PNe positions are shown in Fig. 1.

The spectra were extracted with a Gaussian weight function, whose FWHM is chosen to be $\sim 0''.8$ to approximately match the PSF, providing a S/N-optimised extraction. The apertures were truncated at $2''.4$ to avoid contamination from neighbouring sources. The background was probed locally with identical apertures in eight nearby locations that do not overlap with identified sources. In each channel, we then subtracted the median value of the eight background regions from the source flux (which in-

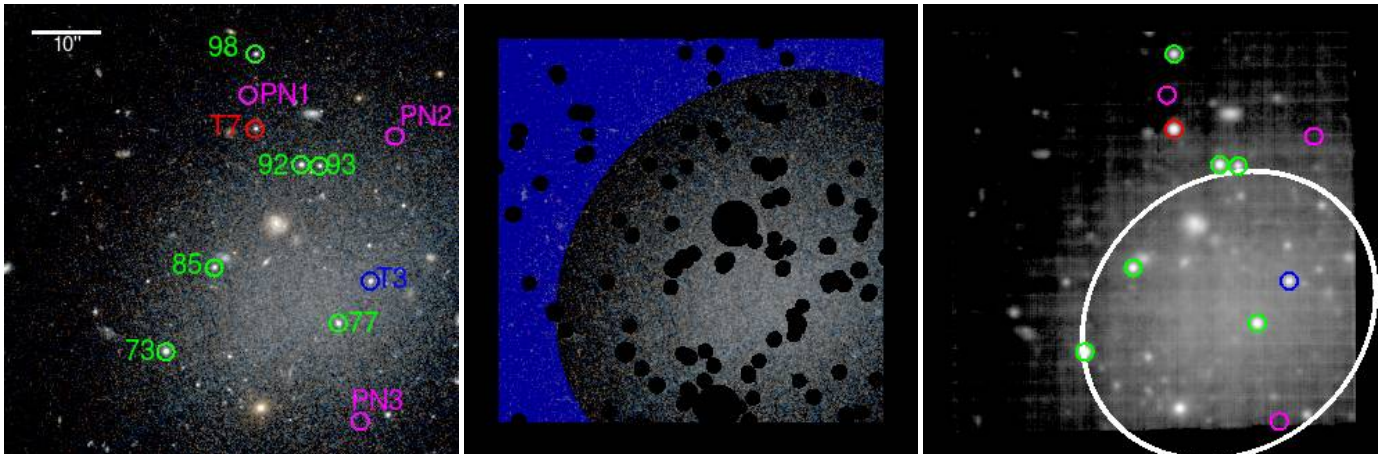


Fig. 1. *Left:* Colour image using F606W and F814 HST imaging over the MUSE field of view. Globular clusters and Planetary Nebulae are indicated. Green circles mark globular clusters identified in van Dokkum et al. (2018c). The blue circle marks a GC candidate from Trujillo et al. (2018) which we confirm to be member of the galaxy based on its velocity, while the red circle marks a GC candidate which, due to its very low systemic velocity, likely is a Galactic foreground star. Purple circles mark PNe with systemic velocities consistent with the galaxy. *Middle:* Same image but with the mask superimposed (in black). The white ellipse marks the region within $1 R_e$, used in this work to extract the main UDG spectrum. The blue region highlights the region used by ZAP to construct the set of sky eigen-spectra. *Right:* MUSE cube stacked using all channels up to 8950 Å that are not masked in our analysis (due to residuals of bright sky lines). The GCs, PNe and UDG region are indicated as before.

cludes the background). The dominant source of uncertainty is thus originating from the scatter in the background spectrum values.

After the sky subtraction performed using ZAP, we extracted the UDG signal in two different ways. The first extraction method, providing a global spectrum, uses the whole MUSE field, and adopting the F814W HST image² as optimal weight function. For this we registered the F814W image to the same 0.2''/pix grid as the MUSE cube, convolved the PSF to match the PSF of the MUSE cube, and identified and masked all compact sources that are detected on this deep broadband image. The mask is shown in Fig. 1. By performing the extraction in each 1.25Å channel separately, we obtained a global UDG spectrum with a S/N peaking at ~ 75 pix⁻¹ at 7000Å, and dropping to ~ 40 pix⁻¹ towards the blue and red end of the spectral range.

We also performed extractions within several elliptical apertures, corresponding to 0.5, 1, 1.5 and 2 times the effective radius R_e as measured along the major axis. We used morphology parameters as measured in van Dokkum et al. (2018c): the UDG centre is taken at RA=40.44542°, Dec=−8.40333°, with axis ratio $b/a = 0.85$, and a position angle of −48° (measured from the North towards the East) from the HST images. The spectrum measured within $1 R_e$ is presented in the top panel of Fig. 2.

We finally built an adaptive spatially binned version of the MUSE datacube, following a Voronoi binning scheme (Cappellari & Copin 2003) with a minimum target signal-to-noise of 15. That binning scheme should reveal any velocity gradient over the MUSE field of view, as well as potential trends along the photometric minor- or major-axes.

2.3. Stellar kinematics

To measure kinematics of the globular clusters and the UDG stellar body, we first construct a wavelength-dependent mask to discard regions where groups of bright sky lines significantly affect

the stellar kinematics. The mask is shown by the greyed-out region in Fig. 2; we use the same mask for the UDG as for the globular clusters.

We extract kinematics mainly with the penalised pixel fitting routine, pPXF, whose principle is described in Cappellari & Emsellem (2004) (see also Cappellari 2017) and is available as a set of python routines³. We use several empirical stellar libraries, including eMiles (Vazdekis et al. 2016; Röck et al. 2016) and Pegase HR (Le Borgne et al. 2004) Single Stellar populations (SSPs), as well as a synthetic set of spectra from Phoenix models (Husser et al. 2013). The eMiles library has the advantage that it covers the full wavelength range of MUSE spectra, and a relatively large set of SSPs built on empirical stellar spectra, but its spectral resolution (2.51 Å FWHM, see Beifiori et al. 2011) in the red is slightly larger than that of the the MUSE spectra. Pegase HR has a significantly higher spectral resolution, while only covering wavelengths up to a bit beyond the H _{α} line. Finally, Phoenix spectra have the advantage to be available at very high resolution and covers the full MUSE spectral range. We thus use eMiles mostly for the determination of radial velocities, with the other two libraries testing the robustness, while we use mostly Phoenix for the velocity dispersion estimations (with Pegase HR and eMiles as testing benches).

2.3.1. Velocities

We derive stellar kinematics with pixel fitting via pPXF and a set of stellar templates. All template spectra are first convolved to the MUSE resolution using the polynomial approximation as in Guérou et al. (2017). All templates and MUSE spectra were then rebinned in logarithm of the wavelength and fed into pPXF. The first step is to derive an optimal (best-fit) stellar template using a selected set of eMiles spectra, constraining the metallicity to be lower than solar. One optimal template is derived using the integrated ($1 R_e$) UDG spectrum, and another template is computed for the clusters via a stacked GC spectrum. For this first step, we

² The HST data are available in the Mikulski Archive for Space Telescopes (MAST; <http://archive.stsci.edu>), under program ID 14644.

³ See <http://www-astro.physics.ox.ac.uk/~mxc/software/>

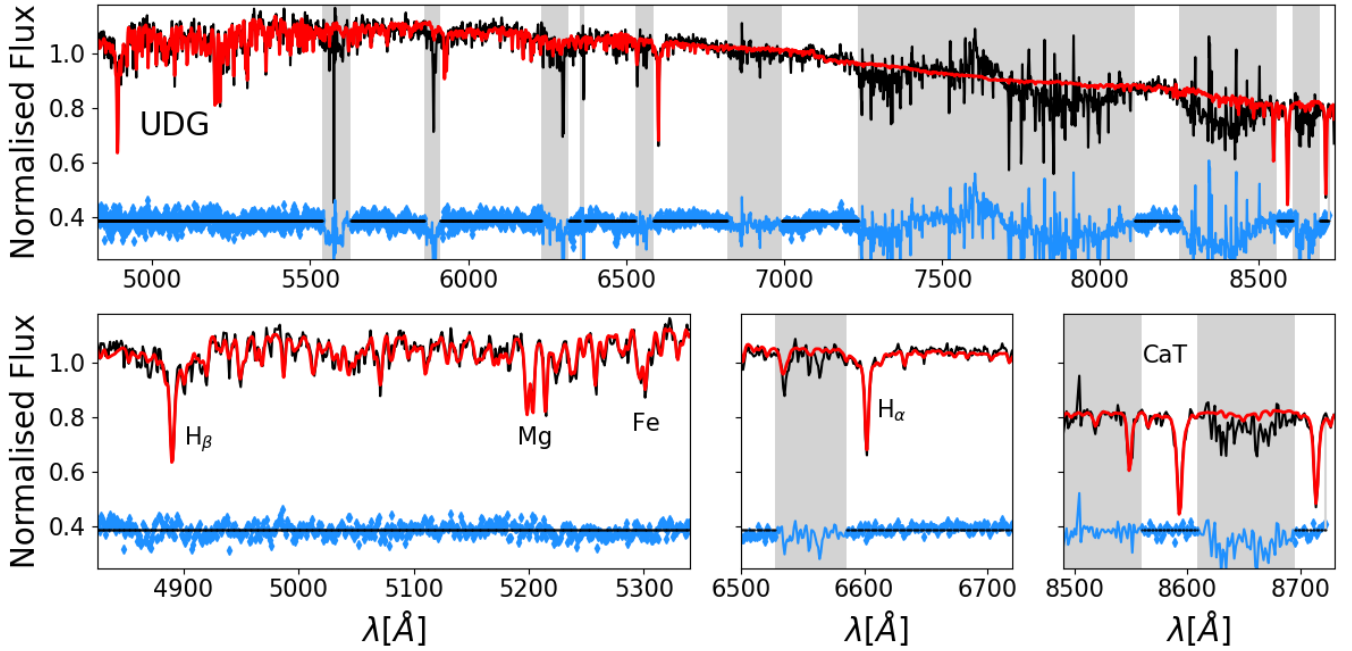


Fig. 2. The UDG spectrum integrated over an aperture of $1 R_e$ (black). The pPXF best fit is shown as a red line, while the residuals are shown as blue dots. The top panel illustrates the full MUSE spectral coverage, while the bottom three panels present zoomed versions around the main stellar absorption lines. Grey regions indicate wavelength ranges that have been excluded from pPXF fitting because of large sky line residuals.

allow for high order multiplicative and additive Legendre polynomials of the 14th and 12th degree, respectively, to correct for differences in the flux calibration and to go beyond limitations of the stellar library.

We then run pPXF to extract stellar velocities, using the respective optimal templates as a single stellar template for the fitting process, still allowing for multiplicative (resp. additive) polynomials of degrees 11 (resp. 4). The uncertainties are estimated by performing 100 realisations of the full spectrum using a *wild bootstrap* methodology (Wu 1986) as in Kacharov et al. (2018).

We have performed several checks to ensure that these velocity measurements are robust. The results are independent of the way the background was subtracted from the MUSE cube (even when ZAP is not used, cf. Appendix A). Also, the degrees of the Legendre polynomials do not significantly affect the results; we checked values between 5 and 14 in steps of 3. The stellar velocities are not significantly affected by the choice of the optimal template (e.g., when we interchange the globular cluster and the UDG template), or even the assumed wavelength dependent spectral resolution (see Sect. 2.3.2), with differences of the order of 0.5 km s^{-1} . We also split the spectra in a blue and red part (centred on 7000\AA): all recovered receding velocities are consistent within uncertainties.

Furthermore, we performed a consistency check of the measured systemic velocities that is independent of the fitting method used; we processed all MUSE spectra via a cross-correlation (CC) method, which is widely used to provide receding velocity measurement of faint galaxies (Tonry & Davis 1979). The CC velocities are also reported with respect to the eMILES spectral library, and for the PNe with respect to a template spectrum generated using optical emission line data provided with the ALFA code (Wesson 2016). All velocity measurements obtained with pPXF and cross-correlations are con-

sistent within less than $1-\sigma$ (cf. Table 1). In the following analysis we adopt the values obtained with pPXF, unless explicitly stated otherwise.

The systemic velocity of the UDG is measured with the best-fit UDG template. We use the same reference template when measuring the systemic velocities in each of the Voronoi bins. We measure the statistical uncertainties in the same way as for the globular clusters, and perform the same robustness tests as before. In all cases, the systematic uncertainties due to different assumptions in the analysis are smaller than the quoted statistical uncertainties. As a note, the use of the Phoenix library of theoretical stellar spectra induces slightly lower velocities, with a systematic difference of 2.0 km s^{-1} , than with eMILES, using the same procedure. This is a systematic shift to both the UDG velocity field and the velocities measured for the GCs, and would only affect the relative velocities with respect to the PNe: such an offset does not affect any of the conclusions drawn in this work.

2.3.2. Velocity dispersions

We expect stellar velocity dispersions for the UDG and clusters typically between 5 and 35 km s^{-1} , which thus represent a substantial fraction of the spectral resolution of the MUSE datacube (σ_{inst} going from ~ 35 to 80 km s^{-1}). To estimate the velocity dispersion of the UDG and the clusters, which are derived relative to convolved templates, we therefore first need to derive precise determinations of the spectral resolution, either parameterised via a wavelength dependent Line Spread Function (LSF), or further approximated with a Gaussian function (via its Full Width at Half Maximum, FWHM hereafter), for both the MUSE datacube and for the reference stellar templates.

As mentioned above, we use a wavelength dependent resolution profile given by a polynomial approximation $\text{FWHM}(\lambda)$, the "UDF10" profile as in Guérou et al. (2017). The lower the

assumed spectral resolution, the higher the resulting estimate for the stellar velocity dispersion. Hence any inaccuracy in the measured profile will bias the estimated velocity dispersions. To take the potential systematic uncertainty on the spectral resolution into account, we use other profiles such as: a direct "LSF" profile, before resampling as given by the MUSE pipeline, as well as the "HDFS" measured profile also mentioned in Guérout et al. (2017). The "LSF" polynomial profile can be considered as providing the upper limits for the velocity dispersions, while the "HDFS" profile should deliver lower limits. We have tested that using a Gaussian approximation for the LSF (via the "LSF" profile) or doing a direct and full LSF convolution of the Phoenix stellar spectra provide consistent results. In the following, we will thus quote results from our nominal "UDF10" profile, while mentioning the limits given mostly by the "LSF" and "HDFS" profiles (the latter having a slightly higher FWHM in the blue than the "UDF10"). We will also focus on the use of the high resolution Phoenix synthetic stellar library as it covers the full MUSE spectral range.

3. Results

3.1. Velocities of globular clusters and planetary nebulae

We measure systemic velocities for six of the clusters that overlap with the sample presented in van Dokkum et al. (2018a), see Table 1. T3 and T7 are globular cluster candidates reported in Trujillo et al. (2018) (and called GCNEW3 and GCNEW7 there) on the basis of their small apparent size and colours. One of those candidates, T3, has a systemic velocity consistent with that of the other globular clusters. The other candidate, T7, has a velocity consistent with a Galactic foreground star: inspecting its MUSE spectrum, we hypothesize that it is an early G-type star.

We compare the measured velocities with those reported in van Dokkum et al. (2018c), and find a systematic offset of $12.5_{-2.5}^{+2.6} \text{ km.s}^{-1}$ when using the eMiles library as a reference (or 14.5 km.s^{-1} when using Phoenix stars). This includes a shift of 5.4 km.s^{-1} due to the different applied redshift-velocity transformation ($c z$ versus $c \ln(1 + z)$ for the present paper). Still, it is more than we expect given the estimated accuracy of our wavelength calibration (cf. Sect. 2.1). The source of this systematic discrepancy is unclear, but we speculate that this may be partly due to the slit effect in the Keck multi-slit data, i.e. non-perfect centering of objects within a slit inherent to multi-object slit observations. During the kinematic studies presented in this paper, we explicitly include this systematic offset as a prior in our likelihood when combining measurements from the two studies.

We also measure systemic velocities for the three PNe, facilitated by their [O III] doublet and H α emission lines, which are detected at high significance (see Fensch et al., Paper II). The measurements and associated errors are reported in Table 1.

3.2. Kinematics and dynamics of the UDG stellar body

The MUSE data set allows us to measure, for the first time, the systemic velocity of the UDG's stellar body. Following the methodology as outlined in Sect. 2.3.1, we measure a systemic velocity of $1792.9_{-1.8}^{+1.4}$ for the spectrum extracted within the effective radius. We measure identical values on the spectrum extracted from the full frame (weighted by the broadband image), as the one extracted within R_e . This value is fully consistent with the mean velocity of the globular clusters (cf. Table 1). The measured velocity provides the rest-frame of the whole system

(which previous studies had to solve for in their likelihood, e.g. Martin et al. 2018; Laporte et al. 2018). We will use this systemic velocity when re-measuring the velocity dispersion of the GC system in Sect. 4. We also find that spectra measured within 0.5, 1.5 or 2.0 R_e all provide consistent velocity values, within 1σ uncertainties (which are of the order of 1.5 km.s^{-1}).

To be able to interpret the measured velocity dispersion of the clusters as a proxy for the dynamical mass of the system, it is important to be aware of any rotational component to the velocity field of the galaxy. van Dokkum et al. (2018c) did not find any evidence for rotation (their Extended Data Figure 5), when they inspected the globular cluster velocities. Fig. 3 presents the MUSE stellar velocity field as derived in the adaptive Voronoi bins of DF2. All obtained bin velocities are within $\pm 6 \text{ km.s}^{-1}$ of the mean systemic velocity, except for one outer bin at $+10 \text{ km.s}^{-1}$, while uncertainties are roughly $\pm 3 \text{ km.s}^{-1}$ (1σ). The MUSE stellar velocity map exhibits a clear trend with positive velocities roughly towards the south and negative velocities mostly towards the north of the centre. The split between (relative) negative and positive velocities seems to be on either side of the photometric major-axis of the galaxy. The strongest detected gradient, evaluated by performing linear fits of the measured velocity with respect to a rotated axis, is along a position angle $\text{PA} = 30^\circ$ (counter-clockwise from north-up axis in Fig. 3), with similar slopes in the PA range $[10^\circ, 47^\circ]$ which includes the photometric minor-axis at $\text{PA} = 42^\circ$: the linear slope is $2.8 \pm 0.9 \text{ km.s}^{-1}$ per $10''$, as illustrated in Fig. 4, with potential large systematic uncertainties due to the shape of the bins and the limited field of view. This measurement is inconsistent with an oblate rotator, while mimicking a system with prolate-like kinematics.

In Fig. 4, we added the above-mentioned linear relation and the residual stellar velocity scatter (1 and 2σ) within the Voronoi bin set. We also derive the circular velocity profiles expected from a simple Sérsic stellar distribution. These are derived from building full three-dimensional models for NGC1052-DF2 via the Multi-Gaussian Expansion formalism (i.e., MGE Emsellem et al. 1994). A projected Sérsic $n = 0.6$ system following morphological parameters (e.g., axis ratio $q = 0.85$) as in van Dokkum et al. (2018c) was fitted with an MGE model and deprojected using different inclination angles θ from edge-on (90°) to close to face-on (35°). We assumed two generic distances as discussed in the literature, namely 20 and 13 Mpc (van Dokkum et al. 2018c; Trujillo et al. 2018), and used a reference stellar mass-to-light ratio of $M/L_V = 2$ van Dokkum et al. (2018c). These profiles are meant as simple guidelines for the measured stellar velocity gradient.

Most GCs and PNe (respectively represented as blue and red symbols in Fig. 4) are consistent with the general uncovered velocity gradient: only one cluster seems to stand out, namely GC93 with its measured relative radial velocity of $\sim +26 \text{ km.s}^{-1}$, very significantly above the main relation, and one out of three PNe (PN3) appears to be an outlier with $\sim -26 \text{ km.s}^{-1}$ with respect to systemic velocity. Assuming a local velocity dispersion of 10 km.s^{-1} (20 km.s^{-1} respectively) and a gaussian velocity distribution, the probability to observe such a high velocity for GC93 or PN3 is $\sim 1\%$ (resp. $\sim 20\%$). This will be discussed further in Sect. 4.1.

3.3. The stellar velocity dispersion of the UDG

We derive a nominal stellar velocity dispersion of $\sigma_{\text{UDG}\star}(R_e) = 16.3_{-4.8}^{+3.4} \text{ km.s}^{-1}$ when using our nominal resolution profile "UDF10" (see Sect. 2.3.2) and the high resolution Phoenix stel-

Table 1. Positions and systemic velocity measurements of the unresolved/point-like sources and the UDG (using the eMiles library). Both results from the fitting method (pPXF) and the cross-correlation (CC) method are given. For the UDG and the GCs, the S/N is measured in the wavelength range [6600Å – 6800Å] in pix^{-1} (one pixel corresponds to a 1.25Å channel). For the PNe the S/N is given for the [O III] $\lambda 5007$ line. First (second) errors on the measured velocities represent statistical (systematic) uncertainties. The latter are the most extreme values obtained given a range of tested templates, background subtraction methods and polynomial degrees of the Legendre function that was fitted to the continuum. For completeness, we augment the table with five GCs which were not covered by our MUSE observations, but for which velocities were reported by vD18 and for which we take the coordinates in Trujillo et al. (2018).

Source	RA [deg]	Dec [deg]	S/N pix^{-1}	V (pPXF) [km/s]	V (CC) [km/s]	vD18 ($c \cdot z$) [km/s]
UDG($< R_e$)	40.44542	-8.40333	75.1	$1792.9^{+1.4+0.2}_{-1.8+1.3}$	$1794.5^{+1.7+0.4}_{-1.5+0.7}$	-
GC73	40.45093	-8.40503	47.6	$1803.8^{+2.8+3.3}_{-3.0+0.7}$	$1803.9^{+2.2+0.7}_{-2.2+0.8}$	1814^{+3}_{-3}
GC77	40.44395	-8.40390	30.7	$1792.6^{+4.4+1.8}_{-4.7+1.6}$	$1787.9^{+3.6+1.2}_{-2.9+1.4}$	1804^{+6}_{-5}
GC85	40.44896	-8.40166	27.1	$1786.3^{+4.3+1.9}_{-4.8+6.1}$	$1786.1^{+3.2+1.5}_{-2.2+0.8}$	1801^{+5}_{-6}
GC92	40.44544	-8.39753	28.9	$1775.5^{+6.2+2.8}_{-4.2+4.7}$	$1772.1^{+2.2+2.3}_{-3.6+4.1}$	1789^{+6}_{-7}
GC93 ^a	40.44469	-8.39759	16.0	$1819.1^{+7.7+21.1}_{-6.8+19.5}$	$1818.6^{+5.5+1.1}_{-6.9+4.4}$	-
GC98 ^b	40.44728	-8.39310	18.0	$1786.3^{+7.4+22.9}_{-11.6+5.7}$	$1782.7^{+9.4+3.7}_{-8.3+4.1}$	1784^{+10}_{-10}
T3 ^c	40.44265	-8.40221	21.6	$1788.7^{+16.9+16.3}_{-10.9-47.7}$	$1794.1^{+5.9+5.1}_{-6.4-10.1}$	-
T7 ^c	40.44729	-8.39610	30.0	22^{+19}_{-16}	52^{+15+15}_{-44-15}	-
PN1	40.44758	-8.39473	20.3	$1790.8^{+2.0}_{-1.8}$	$1790.5^{+2.8+1.4}_{-1.9+1.1}$	-
PN2	40.44164	-8.39639	6.6	$1786.4^{+7.2}_{-5.9}$	$1782.3^{+9.9+2.6}_{-7.5-9.6}$	-
PN3	40.44305	-8.40783	5.8	$1766.4^{+10.2}_{-7.1}$	$1763.3^{+6.9+1.5}_{-5.0-3.5}$	-
GC39	40.43779	-8.42358	-	-	-	1818^{+7}_{-7}
GC59	40.45034	-8.41596	-	-	-	1799^{+16}_{-15}
GC71	40.43807	-8.40638	-	-	-	1805^{+6}_{-8}
GC91	40.42571	-8.39832	-	-	-	1802^{+10}_{-10}
GC101	40.43837	-8.39120	-	-	-	1800^{+13}_{-14}

^a Observed in van Dokkum et al. (2018c) but no measured velocity due to too low S/N in their spectrum.

^b Re-measured value reported in van Dokkum et al. (2018b).

^c Globular cluster candidate reported in Trujillo et al. (2018).

lar library. When using the other resolution profiles, we find dispersion values in the range $[15.9^{+4.1}_{-4.5} - 26.1^{+3.1}_{-3.0}] \text{ km s}^{-1}$.

Such a dispersion measurement mostly relies on a few narrow absorption lines. Extensive tests meant to pin down the effects of various assumptions (spectral domain, resolution profile, degree of additive polynomials) show that it is sensitive to associated changes. Such instabilities are mostly connected with the difficulty to extract small dispersion values while systematics from the assumed LSF and the intrinsic broadening of the relevant absorption lines in different templates (which is linked to the evolutionary stage of the stellar population) are present.

To further assess the robustness of the measured velocity dispersion, we tested the different libraries (Sect. 2.3). We also focused on narrower spectral regions either using the Pegase HR SSP library (for the blue part of the spectrum), or a range around the CaT region where the MUSE spectral resolution is significantly higher than at bluer wavelengths and very close (within 0.1 Å) to e.g., the eMiles library resolution. The drawback is that a slight change in the continuum can affect the relative depth of the lines and the measured dispersion, so that we need to limit the degree of the provided additive polynomials.

The above-mentioned values for $\sigma_{\text{UDG}*}(R_e)$ are consistent with the values derived via the Pegase library, which only covers the region bluewards of 7000 Å, with a nominal dispersion value of $16.3^{+3.4}_{-4.8} \text{ km s}^{-1}$ and a range of $[15.9^{+5.7}_{-7.9} - 26.1^{+3.1}_{-3.0}] \text{ km s}^{-1}$ when varying the resolution profile. When using eMiles, we find values of $13.7^{+1.6}_{-1.4} \text{ km s}^{-1}$ for the full spectral range, and around 6 km s^{-1} when limiting the pixel fit to the CaT region: such values are expected to be underestimates considering that eMiles spectra have a resolution of about 37 km s^{-1} .

(sigma) around the CaT lines, while the expected MUSE spectral resolution is lower with $\sim 35 \text{ km s}^{-1}$. The dispersion restricting the fit bluewards of 7000 Å (where the resolution of the eMiles stellar template is always better than the one of the MUSE spectrum) is fully consistent with our nominal value with $\sigma_{\text{UDG}*}(R_e) = 16.7^{+2.3}_{-1.9}$.

To conclude, we find an nominal value of $\sigma_{\text{UDG}*}(R_e) = 16.3^{+3.4}_{-4.8} \text{ km s}^{-1}$, with typical values ranging from 13 up to 27 km s^{-1} . We note that this measured dispersion includes both ordered and random motions, hence also the rotational component within $1 R_e$.

4. Discussion

4.1. A revised dispersion measurement

We use the set of globular clusters for which we obtained reliable systemic velocities (including two newly measured clusters), the three PNe, and our established central velocity for the entire system to revisit the velocity dispersion measurement of this system. We follow a similar approach as in Martin et al. (2018) and Laporte et al. (2018) to derive the dispersion from a likelihood fit to the kinematic data.

Given that their receding velocities are close to that of the main UDG body, we do assume that all GCs and PNe are part of the galaxy, and we write the likelihood function as

$$\mathcal{L} = \prod_{i=1}^{N_{\text{GC},\text{PN}}=15} \frac{1}{\sqrt{2\pi}\sigma_{\text{obs}}} \exp\left(-0.5\left(\frac{v_i - C_i - v_{\text{sys}}}{\sigma_{\text{obs}}}\right)^2\right), \quad (1)$$

$$\text{with } \sigma_{\text{obs}}^2 = \sigma_{\text{int}}^2 + \sigma_{\text{err}}^2. \quad (2)$$

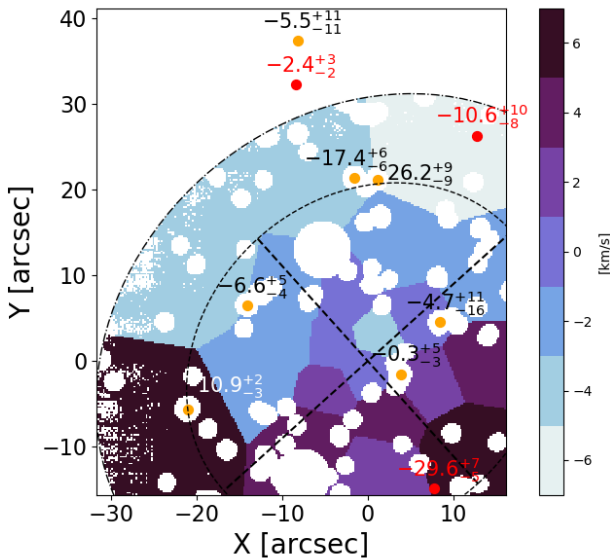


Fig. 3. Stellar velocity field in Voronoi bins of DF2. Orange dots and associated measurements provide the positions and systemic velocities of the seven globular clusters that are members of the galaxy. The velocities are indicated with respect to the systemic velocity of 1793 km/s. The two ellipses correspond to $1 R_e$ and $1.5 R_e$, respectively. The X- and Y axes denote the angular difference with respect to the centre, RA=40.44542°, Dec=−8.40333°, in western and northern direction respectively.

Here, σ_{err} is the measurement uncertainty, σ_{int} is the intrinsic dispersion we are after, and C_i accounts for the velocity calibration offset between our study and that of van Dokkum et al. (2018c). Its value is therefore either 0 (when using tracers measured with MUSE), or an offset value, δ , when we use tracers exclusively reported by van Dokkum et al. (2018c). We measure δ as the offset that minimizes the Least Squares statistic $\sum_i^N (V_{i,\text{vD18}} - \delta - V_{i,\text{MUSE}})^2 / (eV_{i,\text{vD18}}^2 + eV_{i,\text{MUSE}}^2)$, where V and eV are the velocities and velocity uncertainties from both studies. We sum over the five GCs that are observed in common. For the measurements performed with pPXF, we find $\delta = 11.1 \pm 3.0$ ($\delta = 12.3 \pm 2.7$ km/s for the cross-correlation velocities). Since our measurements are more precise than those reported in van Dokkum et al. (2018c), we exclusively use our measurements when available (i.e. when covered by the MUSE field-of-view). The velocity of the system as a whole is v_{sys} . We adopt a uniform prior on $0 < \sigma_{\text{int}} < 30$ km s^{−1}, and a Gaussian prior on v_{sys} based on our MUSE kinematic measurements of the UDG body (cf. Table 1).

We marginalize over c by drawing from a Gaussian distribution with μ and σ according to the velocity calibration offset reported above. We draw 150 times from this distribution and for each draw explore the posterior with ten walkers using emcee (Foreman-Mackey et al. 2013). The combined posterior is shown in Fig. 5. As a consistency check we run the MCMC over the old data set (with uniform prior on $1750 \text{ km/s} < v_{\text{system}} < 1850 \text{ km/s}$, and with the old velocity measurement of GC98) and find a best-fit velocity dispersion of $\sigma_{\text{int}} = 10.2^{+7.0}_{-2.5}$ km/s, which is consistent with Martin et al. (2018) and Laporte et al. (2018). Folding in the additional two globular clusters, three PNe, and constraining the velocity of the system to the UDG mean velocity gives a similar velocity dispersion of $\sigma_{\text{int}} = 10.5^{+4.0}_{-2.2}$ km/s. This assumes that PNe and GCs are equally good tracers of the

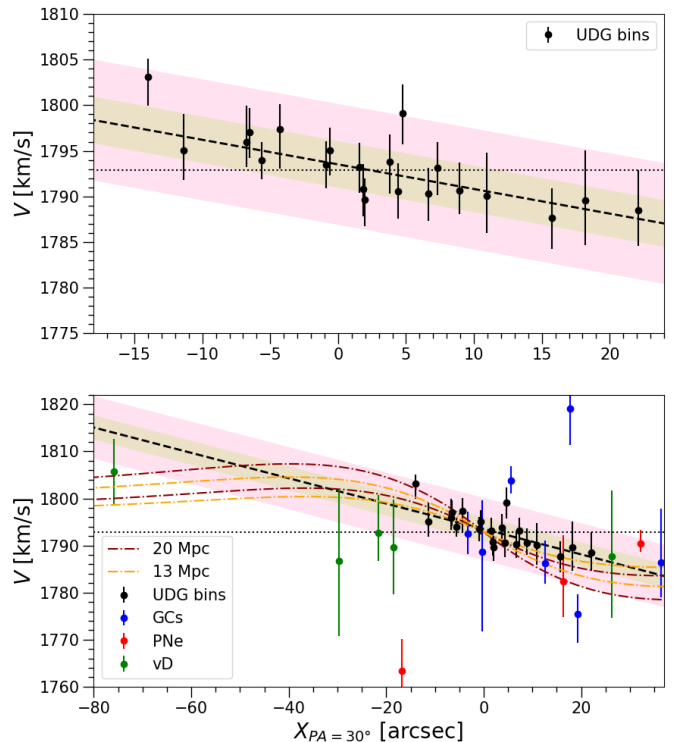


Fig. 4. Stellar velocity field trend shown along a position angle of $+30^\circ$ for the UDG Voronoi bins (in black). The dotted horizontal line shows the systemic velocity derived from the $1 R_e$ elliptical aperture. The dashed line shows the best linear fit on the UDG bins, with the residual scatters (1 and 2.6σ) scatter from the UDG bins alone in shaded green and red. Measured clusters and PNe are respectively shown as blue and red points. The top panel shows a zoom within the MUSE field of view. The bottom panel includes additional clusters measured by van Dokkum et al. (2018c), as well as reference circular velocity profiles from a Sérsic model at a distance of 20 or 13 Mpc with $M/L_V = 2$, and for two different inclination angles (35 and 90° , see text).

potential and are all drawn from distribution functions with comparable LOS dispersions. Velocities from the cross-correlation method yield $\sigma_{\text{int}} = 12.3^{+5.0}_{-1.4}$ km/s. We note that the results above are not corrected for small-sample bias as per Laporte et al. (2018). With the current uncertainties, this would increase the inferred dispersions σ_{int} by $\approx 10\%$.

This estimate is affected by the global velocity trend shown in Fig. 4. Here we estimate the velocity dispersion with the same method after subtracting the global velocity trend for the 15 tracers. Since PNe have stellar progenitors, one would expect them to follow the stellar field dynamically. The GCs, while sharing the same potential, may be on very different orbits (e.g., have a different anisotropy and/or volume occupation). Indeed, the dispersion measured around the five trends plotted in Fig. 4 range from 11.2 - 13.6 km/s, as opposed to the nominal value of $\sigma_{\text{int}} = 10.5^{+4.0}_{-2.2}$ km/s. Given the uncertainties associated with our limited set of 15 tracers we find no significant evidence that their kinematics is the same as (or differs from) the trend observed in the stellar body. The velocity dispersion as estimated using the 15 tracers is lower than the velocity dispersion of the UDG stellar body as reported in Sect. 3.2, though consistent within uncertainties (see also Laporte et al. 2018).

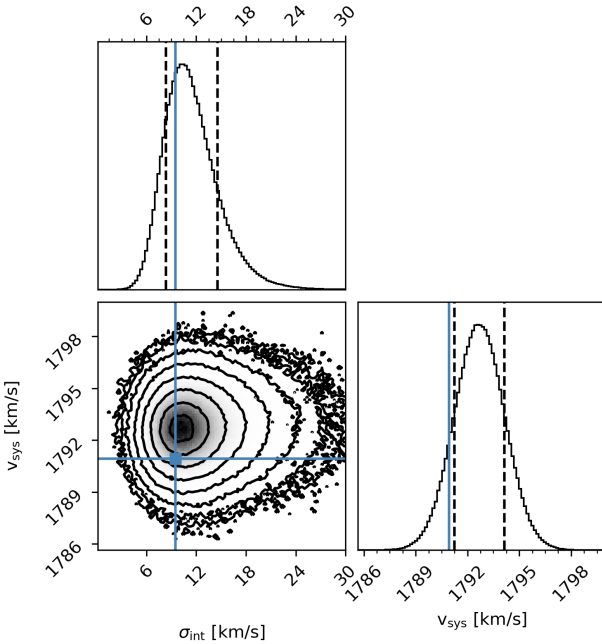


Fig. 5. Inference on systemic velocity and internal velocity dispersion using discrete kinematical tracers. The blue point is the old measurement (Martin et al. 2018, shifted by the velocity calibration bias) before v_{sys} , velocities of two additional GCs and three PNe were measured.

4.2. The UDG dynamical mass

We now turn to the estimate of the mass of the UDG using several estimators and either the velocity dispersion of the discrete tracers (GC and PNe, see previous Section) or the stellar velocity dispersion of the UDG (Sect. 3.3). The two dispersion values are consistent with each other within the derived uncertainties. As already emphasised, we do not necessarily expect them to exactly agree for at least two reasons : 1- these measurements do not cover the same physical (radial) range, with σ_{int} including tracers up to $\sim 80''$ or $\sim 3.5 R_e$, while $\sigma_{\text{UDG}\star}(R_e)$ was defined with one effective radius; 2- the small number of discrete measurements with relatively large uncertainties may lead to a significant under (or over-) estimate plus a systematic bias, as emphasised by Laporte et al. (2018).

Recent mass estimators via the inferred effective radius R_e and the associated velocity dispersion σ_{los} (within $1 R_e$) use relations proportional to $R_e G^{-1} \sigma_{\text{los}}$, with varying multiplicative constants. A recent estimator was provided by Errani et al. (2018) with $M(< 1.8 R_e) = 6.3 \cdot R_e G^{-1} \langle \sigma_{\text{los}} \rangle$ (see also the earlier and similar estimator in Amorisco & Evans 2011). This would lead to masses (within $1.8 R_e$) of $3.5^{+3.2}_{-1.3} 10^8 M_\odot$ and $8.5^{+3.9}_{-4.2} 10^8 M_\odot$ when using σ_{int} and $\sigma_{\text{UDG}\star}(R_e)$ respectively, and mass-to-light ratios M/L_V of $3.4^{+3.1}_{-1.3}$ (resp. $8.3^{+3.8}_{-4.2}$) assuming Newtonian dynamics and a distance of 20 Mpc. Following Courteau et al. (2014) (see their Sect. 5.2, and Table 2 of that Section), we can also write an estimate of the mass within one effective radius as $M(R_e) = 4 \cdot R_e G^{-1} \sigma_{\text{los}}$ (see also Wolf et al. 2010), and this would lead to 10% higher values for M/L_V . A closer distance of 13 Mpc would significantly increase the above-mentioned M/L by about 55% (as M/L is inversely proportional to the assumed distance), with M/L_V of 5.3 and 12.7 when using the GCs and PNe, or the UDG stellar body.

A second way forward to estimate the dynamical mass of the UDG is to use Jeans modelling and predictions for the velocity dispersion of the UDG within $1 R_e$. We thus apply the MGE formalism mentioned in Sect. 3.2 and solve the Jeans equations producing N-body realizations for a Sersic $n = 0.6$ stellar body as in Emsellem (2013). Varying the anisotropy and inclination, we obtain direct predictions for the observed stellar velocity dispersion $\sigma_{\text{dyn}}(R_e)$ and can compare these with the observed MUSE value. Assuming a distance of 20 Mpc, and inclination angles between 90° (edge-on view) and 35° (close to face-on view), we derive corresponding M/L_V between ~ 8 and $8.8 (\pm 4)$ to reproduce the 16.3 km s^{-1} stellar dispersion, consistent within 10% with the ones provided above via direct mass estimators. This scales to M/L_V from ~ 12.4 to 13.6 when using a distance of 13 Mpc. A mass-to-light ratio of 8 within $1 R_e$ corresponds to a mass of $\sim 4.4 \cdot 10^8 M_\odot$ within that radius.

Finally, it is worth noting that the new estimates of the velocity dispersions, both from the discrete tracers or the stellar body of the UDG, are in broad agreement with the MOND prediction, once the external field effect is properly taken into account (Famaey et al. 2018), as they predicted $\sigma_{\text{MOND}} = 13.4^{+4.8}_{-3.7} \text{ km s}^{-1}$ (also cf. Kroupa et al. 2018).

4.3. On the origin of DF2

The stellar velocity field of the UDG (see Sect. 3.2) is clearly not consistent with a simple oblate axisymmetric system. The galactic kinematic axis is closer to the minor than the major photometric axis of DF2, making this a prolate-like rotation field. Such structures are not unheard of for low luminosity galaxies (see e.g. Ho et al. 2012; Kacharov et al. 2017).

The origin of such systems has been discussed over the last decade with help from numerical simulations. Several scenarios were put forward. Firstly, an accretion event or major merger may be an efficient way to produce prolate-like rotation (Amorisco et al. 2014; Łokas et al. 2014; Fouquet et al. 2017), something that was also called upon for massive galaxies (see e.g. Krajnović et al. 2018; Graham et al. 2018; Ene et al. 2018) backed up by numerical simulations (e.g. Velliscig et al. 2015; Li et al. 2016; Ebrová & Łokas 2017; Li et al. 2018). Secondly, in the case of DF2, another process could be tidal stirring by a more massive nearby galaxy. Simulations by e.g. Łokas et al. (2010) have shown that tides by a massive host can drive the density of a dwarf to triaxial configurations, and result in prolate-like kinematic signatures. Simulations by Ogiya (2018) suggest that tidal stripping on a radial orbit could explain the main morphological parameters of NGC1052-DF2 and a lowered amount of dark matter in such a processed stellar system, but that study does not comment on the internal kinematics. More generally, prolate and triaxial systems arise naturally due to tides, as has been shown by e.g. Varri & Bertin (2009) by using self-consistent distribution functions in external tidal fields. This simply derives from the fact that Roche lobes are triaxial.

One hint that the galaxy may be perturbed and not phase-mixed is the detection by Trujillo et al. (2018) of an extended surface brightness feature towards the north in their very deep Gemini *g*-band image. We may further speculate that the discrepant velocities for PN3 (and possibly GC93) are associated with a dynamical disturbance.

5. Summary and conclusions

We have presented the first kinematic study of the stellar body of NGC 1052-DF2, using new integral-field spectroscopy from

MUSE. This is the first time that MUSE was used to measure the kinematics of a galaxy at such low surface brightness. Its large field of view allows us to study, at the same time, the global kinematics of the stellar body, and the systemic velocities of point sources such as globular clusters and nebular emitters. Systematics are discussed, focused primarily on a treatment of the dominating sky background in the MUSE data cube.

We find that the receding velocity of the UDG is consistent with that of the mean globular cluster velocity. We reveal a significant velocity gradient throughout the MUSE field of view of about $\pm 6 \text{ km s}^{-1}$ within a radius of $\sim 20''$. The stellar velocity map is not consistent with a simple oblate rotator. The kinematic major-axis is offset by about 70° from the photometric major-axis, making this system a prolate-like rotator.

We measure spectra for seven globular clusters with high-enough S/N to be able to measure a reliable systemic velocity. Another compact source, with broadband colours consistent with a globular cluster is confirmed to be a Galactic foreground star (likely a G-type star). We also for the first time detect the presence of three PNe within a UDG, and derive their radial velocities, two of them being in line with the UDG stellar kinematics.

We provide two velocity dispersion measurements, one from the set of clusters and one of the stellar body. First, we revise the velocity dispersion reported in the literature for this system, which was based on 10 globular clusters. Folding in 1) two additional measured globular cluster velocities, 2) improved measurements for five others, 3) three PNe under the assumption that they are similar tracers of the potential, and 4) a precisely-determined mean velocity of the whole system, we find a velocity dispersion of $\sigma_{\text{int}} = 10.5^{+4.0}_{-2.2} \text{ km/s}$. Second, we measure for the first time the stellar velocity dispersion of the UDG stellar body with $\sigma_{\star}(R_e) = 16.3^{+3.4}_{-4.8} \text{ km s}^{-1}$, with lower (resp. upper) limits of 13 km s^{-1} (resp. 26 km s^{-1}) when accounting for systematics.

While the dispersion estimates based on the stellar body and that of the discrete tracers are consistent, an interpretation of these measurements in terms of whether the galaxy is, or is not, dominated by a dark-matter component still awaits a robust measurement of its distance.

In a companion paper (Paper II, Fensch et al. submitted), we study the stellar populations of this UDG, compare it to the stellar populations of the globular clusters in this system and discuss the origin of this galaxy.

Acknowledgements. We thank Magda Arnaboldi, Souradeep Bhattacharya, and Glenn van de Ven for helpful discussions. RvdB thanks the participants of Lorentz Centre Workshop “The Bewildering Nature of Ultra-diffuse Galaxies” for insightful discussions. We thank Lodovico Coccato for his extremely useful help on the use of ZAP. We thank Simon Conseil for useful correspondence on the use of ZAP, Laure Piqueras for her insight and support regarding mpdaf and both for general feedback on MUSE data reduction related topics. Analysing the MUSE data and writing the paper, we made use of Astropy (Astropy Collaboration et al. 2013), with heavy usage of the Python packages NumPy (Walt et al. 2011), iPython (Prez & Granger 2007), SciPy (Jones et al. 2001), matplotlib (Hunter 2007), mpdaf (Piqueras et al. 2017), emcee (Foreman-Mackey et al. 2013) as well as Spectres (Carnall 2017) and pPXF (Cappellari & Emsellem 2004; Cappellari 2017). We would thus like to thank all who designed and contributed to these excellent pieces of software, and most importantly made them available to the community.

References

Amorisco, N. C. & Evans, N. W. 2011, MNRAS, 411, 2118
 Amorisco, N. C., Evans, N. W., & van de Ven, G. 2014, Nature, 507, 335
 Battaglia, G., Helmi, A., & Breddels, M. 2013, New A Rev., 57, 52
 Beifiori, A., Maraston, C., Thomas, D., & Johansson, J. 2011, A&A, 531, A109
 Cappellari, M. 2017, MNRAS, 466, 798
 Cappellari, M. & Copin, Y. 2003, MNRAS, 342, 345
 Cappellari, M. & Emsellem, E. 2004, PASP, 116, 138
 Carnall, A. C. 2017, arXiv e-prints
 Clauwens, B., Schaye, J., Franx, M., & Bower, R. G. 2018, MNRAS, 478, 3994
 Courteau, S., Cappellari, M., de Jong, R. S., et al. 2014, Reviews of Modern Physics, 86, 47
 Ebrová, I. & Łokas, E. L. 2017, ApJ, 850, 144
 Emsellem, E. 2013, MNRAS, 433, 1862
 Emsellem, E., Monnet, G., & Bacon, R. 1994, A&A, 285, 723
 Ene, I., Ma, C.-P., Veale, M., et al. 2018, MNRAS, 479, 2810
 Errani, R., Peñarrubia, J., & Walker, M. G. 2018, MNRAS, 481, 5073
 Famaey, B., McGaugh, S., & Milgrom, M. 2018, MNRAS, 480, 473
 Foreman-Mackey, D., Hogg, D. W., Lang, D., & Goodman, J. 2013, PASP, 125, 306
 Fouquet, S., Łokas, E. L., del Pino, A., & Ebrová, I. 2017, MNRAS, 464, 2717
 Graham, M. T., Cappellari, M., Li, H., et al. 2018, MNRAS, 477, 4711
 Guérou, A., Emsellem, E., McDermid, R. M., et al. 2015, ApJ, 804, 70
 Guérou, A., Krajnović, D., Epinat, B., et al. 2017, A&A, 608, A5
 Hayashi, K. & Inoue, S. 2018, MNRAS
 Ho, N., Geha, M., Muñoz, R. R., et al. 2012, ApJ, 758, 124
 Husser, T.-O., Wende-von Berg, S., Dreizler, S., et al. 2013, A&A, 553, A6
 Kacharov, N., Battaglia, G., Rejkuba, M., et al. 2017, MNRAS, 466, 2006
 Kacharov, N., Neumayer, N., Seth, A. C., et al. 2018, MNRAS, 480, 1973
 Krajnović, D., Emsellem, E., Cappellari, M., et al. 2011, MNRAS, 414, 2923
 Krajnović, D., Emsellem, E., den Brok, M., et al. 2018, MNRAS, 477, 5327
 Kroupa, P., Hagh, H., Javanmardi, B., et al. 2018, Nature, 561, E4
 Laporte, C. F. P., Agnello, A., & Navarro, J. F. 2018, MNRAS in press
 Le Borgne, D., Rocca-Volmerange, B., Prugniel, P., et al. 2004, A&A, 425, 881
 Lelli, F., Fraternali, F., & Verheijen, M. 2014, A&A, 563, A27
 Li, H., Li, R., Mao, S., et al. 2016, MNRAS, 455, 3680
 Li, H., Mao, S., Emsellem, E., et al. 2018, MNRAS, 473, 1489
 Łokas, E. L., Ebrová, I., Pino, A. d., & Semczuk, M. 2014, MNRAS, 445, L6
 Łokas, E. L., Kazantzidis, S., Majewski, S. R., et al. 2010, ApJ, 725, 1516
 Martin, N. F., Collins, M. L. M., Longeard, N., & Tollerud, E. 2018, ApJ, 859, L5
 Mayer, L. 2011, in EAS Publications Series, Vol. 48, EAS Publications Series, ed. M. Koleva, P. Prugniel, & I. Vauglin, 369–381
 McConnachie, A. W. 2012, AJ, 144, 4
 Ogiya, G. 2018, MNRAS, 480, L106
 Oman, K. A., Marasco, A., Navarro, J. F., et al. 2019, MNRAS, 482, 821
 Oser, L., Ostriker, J. P., Naab, T., Johansson, P. H., & Burkert, A. 2010, ApJ, 725, 2312
 Piqueras, L., Conseil, S., Shepherd, M., et al. 2017, arXiv e-prints, arXiv:1710.03554
 Röck, B., Vazdekis, A., Ricciardelli, E., et al. 2016, A&A, 589, A73
 Skillman, E. D. 2012, Astrophysics and Space Science Proceedings, 28, 3
 Soto, K. T., Lilly, S. J., Bacon, R., Richard, J., & Conseil, S. 2016, MNRAS, 458, 3210
 Toloba, E., Guhathakurta, P., Peletier, R. F., et al. 2014, ApJS, 215, 17
 Tonry, J. & Davis, M. 1979, AJ, 84, 1511
 Trujillo, I., Beasley, M. A., Borlaff, A., et al. 2018, ArXiv e-prints
 van Dokkum, P., Cohen, Y., Danieli, S., et al. 2018a, ApJ, 856, L30
 van Dokkum, P., Cohen, Y., Danieli, S., et al. 2018b, Research Notes of the American Astronomical Society, 2, 54
 van Dokkum, P., Danieli, S., Cohen, Y., et al. 2018c, Nature, 555, 629
 van Dokkum, P., Danieli, S., Cohen, Y., Romanowsky, A. J., & Conroy, C. 2018d, ApJ, 864, L18
 Varri, A. L. & Bertin, G. 2009, ApJ, 703, 1911
 Vazdekis, A., Koleva, M., Ricciardelli, E., Röck, B., & Falcón-Barroso, J. 2016, MNRAS, 463, 3409
 Velliscig, M., Caccioli, M., Schaye, J., et al. 2015, MNRAS, 453, 721
 Wesson, R. 2016, MNRAS, 456, 3774
 Wolf, J., Martinez, G. D., Bullock, J. S., et al. 2010, MNRAS, 406, 1220
 Wu, C. F. J. 1986, Ann. Statist., 14, 1261

Appendix A: Robustness of sky subtraction method

For a correct interpretation of our results, it is essential that the UDG signal is robustly separated from the sky signal. Especially in the low-surface brightness regime in which we are operating, this can be a challenge. Here are the three important parameters for the sky subtraction computation:

- Mask of the UDG: one needs to use a mask for which enough sky is available to well sample the variation of the LSF over the field of view and reduce the noise of the method, with the least possible contamination from the UDG. We used a series of elliptical masks and chose the size corresponding to a convergence of the extracted flux of the UDG and to the rise of noise (circularized radius: 30''). This is the mask shown in the middle panel of Fig 1. In order to verify that the size of the mask does not affect the result, we also analyzed cubes created with a larger masking of the UDG, using a circularized radius of 36''.

- Number of eigenvectors: by default, ZAP chooses the optimal number of eigenvectors to subtract to the data cube, by looking at the inflexion point of the variance curve. For our cube, ZAP computed that 80 eigenvectors are the optimal value. However, the higher the number of eigenvectors, the higher the probability to remove signal from the source. We studied the evolution of the extracted spectra with the number of eigenvectors and found a convergence starting at 30 eigenvectors. In order to verify the effect of this parameter on the results, we analyzed cubes with three different number of eigenvectors: 30, 45 and 60.

- Window for the continuum subtraction: before computing the singular value decomposition and the eigenvalues, ZAP filters out the continuum using a weighted median filter in a moving window whose size is chosen by the user. [Soto et al. \(2016\)](#) found that a width of 20-50 pixels is optimal. We extract spectra using a range of values and found a convergence for widths between 30 and 50 pixels. In order to verify the effect of this parameter on the results, we analyzed cubes with two different window sizes: 30 and 50 pixels.

Thus we analyzed 12 cubes, each with a different set of parameters for the ZAP sky reduction process. The resulting velocity measurements are all included in the systematic uncertainties quoted in the main Tables of this work.

As a final test we also apply a method to subtract the sky background which is completely independent from ZAP, hereafter called “conventional” sky subtraction. For this we use a galaxy template that is constructed from the HST F814W image. We re-grid this image to the same pixel grid as the MUSE cube and convolve the data to the same PSF as the MUSE image quality. We fit this template to each wavelength channel independently. In addition to this we fit a constant (i.e. a plane) to represent the sky background emission in each channel. As expected, this method works well in regions that are devoid of bright sky emission lines.

As a robustness test we have run our kinematic analysis on the cube with the “conventional” sky subtraction. Whereas the spectra are cosmetically less clean than those extracted from the ZAPped cubes, the differences occur mostly near bright sky lines; in these regimes ZAP performs remarkably better. However, those spectral regions are masked when performing our kinematic measurements, and we find that none of the derived velocities are significantly changed compared to extractions from the ZAPped cubes. The systematic differences are included in the second errors that are quoted in Table 1.

Appendix B: Kinematics of NGC1052-DF2

We provide here (Table B.1) the list of Voronoi bins used to map the kinematics of NGC1052-DF2, and the associated velocities, including values both from pPXF and cross-correlation methods.

Table B.1. Positions and systemic velocity measurements of the UDG in Voronoi bins (using the eMiles library). There are 21 bins, for which we provide the relative positions of the nodes and corresponding velocities as measured with the pPXF fitting and cross-correlation methods. The X- and Y coordinates refer to angular offsets with respect to the centre, RA=40.44542°, Dec=−8.40333°, in western and northern direction respectively. In columns 5 and 6 (minV, maxV) we also provide systematics when using various setups for the sky subtraction (see App. A).

Bin	X node [arcsec]	Y node [arcsec]	V (pPXF) [km/s]	V (CC) [km/s]
1	-0.10	-1.09	1793.5 ^{+2.5} _{-2.6} ^{+0.8} _{-1.1}	1795.4 ^{+5.2} _{-2.1} ^{+2.6} _{-2.8}
2	-4.09	2.01	1793.8 ^{+3.0} _{-3.5} ^{+1.1} _{-1.1}	1797.5 ^{+3.0} _{-3.0} ^{+2.6} _{-3.3}
3	-2.60	6.97	1793.1 ^{+2.9} _{-3.0} ^{+0.5} _{-0.8}	1794.9 ^{+0.7} _{-5.4} ^{+2.1} _{-2.1}
4	-8.59	7.65	1790.1 ^{+4.7} _{-4.1} ^{+0.5} _{-2.9}	1793.2 ^{+6.4} _{-4.8} ^{+2.8} _{-2.2}
5	-9.22	2.36	1790.3 ^{+2.8} _{-3.0} ^{+0.7} _{-1.9}	1790.5 ^{+2.5} _{-2.9} ^{+1.4} _{-5.4}
6	-4.77	-3.42	1795.1 ^{+2.5} _{-2.7} ^{+0.5} _{-0.8}	1795.7 ^{+4.1} _{-2.2} ^{+1.8} _{-3.6}
7	2.48	-6.35	1796.0 ^{+4.0} _{-2.7} ^{+0.1} _{-0.5}	1796.7 ^{+2.6} _{-4.3} ^{+1.2} _{-1.5}
8	-11.89	-1.79	1790.5 ^{+3.1} _{-3.0} ^{+1.0} _{-1.7}	1791.3 ^{+3.5} _{-4.9} ^{+2.2} _{-5.2}
9	-19.05	10.00	1789.6 ^{+3.4} _{-3.9} ^{+0.7} _{-3.5}	1793.2 ^{+2.3} _{-3.4} ^{+4.7} _{-8.0}
10	-21.88	-7.17	1799.1 ^{+3.2} _{-3.4} ^{+0.8} _{-2.8}	1801.7 ^{+3.7} _{-3.5} ^{+0.8} _{-0.8}
11	-5.98	-8.40	1797.3 ^{+2.8} _{-4.3} ^{+0.5} _{-2.1}	1798.2 ^{+2.5} _{-3.3} ^{+1.8} _{-3.7}
12	1.16	2.95	1789.6 ^{+2.3} _{-2.9} ^{+0.5} _{-1.9}	1790.2 ^{+4.0} _{-4.4} ^{+1.0} _{-4.0}
13	-7.13	21.40	1788.5 ^{+4.4} _{-3.9} ^{+1.9} _{-2.6}	1792.1 ^{+2.8} _{-2.8} ^{+4.1} _{-4.0}
14	4.00	12.60	1790.6 ^{+3.1} _{-3.3} ^{+0.7} _{-1.2}	1792.1 ^{+2.8} _{-2.8} ^{+4.2} _{-4.0}
15	5.67	5.11	1793.2 ^{+2.8} _{-3.0} ^{+0.4} _{-0.1}	1793.6 ^{+2.8} _{-3.0} ^{+0.8} _{-0.8}
16	1.24	-12.40	1795.1 ^{+3.0} _{-3.0} ^{+0.4} _{-0.1}	1798.6 ^{+1.8} _{-3.0} ^{+1.8} _{-1.8}
17	7.29	-2.28	1793.9 ^{+3.3} _{-3.1} ^{+0.7} _{-0.9}	1794.5 ^{+0.4} _{-4.4} ^{+1.8} _{-1.8}
18	8.61	23.13	1787.6 ^{+3.1} _{-3.3} ^{+0.2} _{-0.1}	1789.1 ^{+4.4} _{-4.4} ^{+2.8} _{-3.9}
19	12.55	9.36	1790.8 ^{+3.0} _{-2.6} ^{+0.8} _{-0.0}	1789.4 ^{+3.3} _{-3.5} ^{+0.9} _{-0.9}
20	12.77	-0.15	1797.1 ^{+2.9} _{-2.9} ^{+1.1} _{-1.1}	1798.2 ^{+2.6} _{-5.4} ^{+0.4} _{-2.1}
21	11.18	-9.71	1803.1 ^{+2.0} _{-3.2} ^{+0.7} _{-1.1}	1803.6 ^{+4.1} _{-2.6} ^{+5.4} _{-1.8}